Computers and Electronics in Agriculture 123 (2016) 362–375

Contents lists available at ScienceDirect

Computers and Electronics in Agriculture

journal homepage: www.elsevier.com/locate/compag

Original papers

Robust visual servo control in the presence of fruit motion for robotic citrus harvesting ☆

S.S. Mehta [a,*], W. MacKunis [b], T.F. Burks [c]

[a] Department of Industrial and Systems Engineering, University of Florida, Shalimar, FL 32579, United States
[b] Physical Sciences Department, Embry-Riddle Aeronautical University, Daytona Beach, FL 32114, United States
[c] Department of Agricultural and Biological Engineering, University of Florida, Gainesville, FL 32611, United States

ARTICLE INFO

Article history:
Received 7 October 2015
Received in revised form 2 March 2016
Accepted 6 March 2016
Available online 21 March 2016

Keywords:
Vision-based control
Robotic harvesting
Agricultural robotics
Fruit motion

ABSTRACT

Unknown fruit motion due to exogenous disturbances such as wind gust, canopy unloading, and particularly, fruit detachment forces can reduce overall harvesting efficiency in robotic fruit harvesting. Existing approaches relying on high-gain controllers to compensate for fruit motion are inherently susceptible to measurement noise and can lead to instability. The contribution of this paper is in the development of a robust image-based visual servo controller to regulate a robotic manipulator to a target fruit in the presence of unknown fruit motion. The robust feedback elements included in the control structure compensate for non-vanishing nonlinear disturbances without the need for high-gain feedback. Lyapunov-based stability analysis guarantees uniformly ultimately bounded regulation of the robot end-effector to a target fruit. In addition, finite-time convergence analysis is presented to show that the controller gains can be chosen to achieve the desired fruit removal rate, or cycle time. Numerical simulations with varying fruit displacement of $\{35, 70, 105, 140, 175, 210\}$ mm verify the feasibility of the developed controller while the performance is evaluated on a seven degrees-of-freedom kinematically redundant manipulator using an artificial citrus fruit moving with 120 mm displacement. The developed robust controller demonstrates stable closed-loop operation of the system. Further, the effect of uncertainties in field conditions such as illumination variations and partial fruit occlusion, overlapping fruit, and obstacles on the developed controller are discussed.

1. Introduction

Robotic harvesting is a viable solution to fresh fruit harvesting in developed countries due to high labor costs and limited availability of seasonal labor. The first major program in robotic fruit harvesting was started at the University of Florida in the 1980s (Harrell et al., 1990a,b). Subsequently, numerous researchers around the world studied robotic solutions for fresh market fruit as well as vegetable harvesting. A comprehensive review of robotic systems in agriculture can be found in Tillett (1993), Sarig (1993), Hannan and Burks (2004), Li et al. (2011), and Bac et al. (2014). Sarig (1993) identified the major challenges in robotic harvesting as fruit recognition, localization, and detachment. Although still active fields of interest, fruit identification and localization problems are well-studied, cf. Jimenez et al. (2000) and Li et al. (2011). Fruit detachment or removal requires guiding a robotic manipulator to the identified fruit position and using an appropriate method for stem severing. Visual servo controllers are commonly used to regulate a robot to a target fruit for harvesting using image feedback from a single or multiple cameras and, often, using an estimate of the fruit depth. However, one of the practical challenges in citrus harvesting is that the fruit may not be stationary. Exogenous disturbances such as wind gusts, fruit detachment forces, canopy unloading, and robot-tree contact cause an unknown time-varying fruit motion, which aggravates for fruits with longer stems. If not considered during control system development, the fruit motion could result in unsuccessful pick cycle and reduce the overall harvesting efficiency.

Robotic harvesters using open-loop servo control or dead-reckoning (d'Esnon, 1985; Levi et al., 1988; Ceres et al., 1998) are highly vulnerable to fruit motion since fruit position is not updated

☆ This research is supported in part by a grant from the United States Department of Agriculture Small Business Innovation Research (USDA-SBIR) award #2012-33610-19499 and the USDA NIFA AFRI National Robotics Initiative #2013-67021-21074. Any opinions, findings and conclusions or recommendations expressed in this material are those of the author(s) and do not necessarily reflect the views of the funding agency.

* Corresponding author.
E-mail addresses: siddhart@ufl.edu (S.S. Mehta), william.mackunis@erau.edu (W. MacKunis), tburks@ufl.edu (T.F. Burks).

http://dx.doi.org/10.1016/j.compag.2016.03.007
0168-1699/

during the reaching stage. The limitation of dead-reckoning to fruit motion can be overcome by employing continuous time fruit position feedback. The Florida Citrus Picking Robot by Harrell et al. (1989), Harrell et al. (1990a,b) used a closed-loop controller with camera-in-hand (CIH) configuration and an ultrasound transducer for range measurement. Concerns existed regarding the stability of the closed-loop system because the control gains surged as the robot neared a fruit. Although compensation was offered through gain scheduling, rigorous performance guarantees were not provided. Rabatel et al. (1995) and Juste and Sevila (1991) considered only image feedback from a monocular camera to servo manipulator along the optical ray (i.e., line-of-sight) to a target fruit. The lack of knowledge of distance to fruit was identified as a concern. In Muscato et al. (2005), the CRAM citrus harvester used differential image size of the fruit for depth identification with line-of-sight based controller. In our previous work (Mehta and Burks, 2014b), an exponentially stable controller was developed to guarantee the desired transient performance (e.g., pick cycle time). Visual servo control for non-citrus fruit harvesting using monocular, stereo, and cooperative camera system has also been studied, e.g., tomatoes (Buemi et al., 1996; Kondo et al., 1996), eggplants (Hayashi et al., 2002), apples (Baeten et al., 2008; De-An et al., 2011), and cucumbers (Van Henten et al., 2002; Van Henten et al., 2003). The existing approaches to vision-based robotic harvesting either do not consider fruit motion or rely on high-gain controllers (Mehta and Burks, 2014b) in conjunction with or separate from high-frequency camera feedback (Harrell et al., 1989; Harrell et al., 1990a,b) for fruit motion compensation. Approaches using high-gain controllers are susceptible to measurement noise as inadvertently noise gets amplified along with the feedback signal, which could lead to high-bandwidth actuation (causes chattering of the end-effector) and system instability. In the field conditions, where a fruit can easily be partially occluded or clustered, additional image processing becomes necessary to robustly identify the fruit to improve fruit detection rates, which limits the rate of image feedback. Passive approach to fruit motion compensation using high frequency image feedback may not be viable with the need for robust image processing (Muscato et al., 2005) and the desire to process higher resolution imagery for improved positioning accuracy. Additionally, since disturbance dynamics are not taken into account, passive approaches fail to guarantee stability and performance of the closed-loop harvesting system. Various researchers (Fortuna et al., 1996; Hayashi et al., 2002; Muscato et al., 2005; Mehta and Burks, 2014b; Bac et al., 2014) have expressed the need for robust and adaptive control methods to improve harvesting efficiency when uncertainties in fruit detection and tracking arise.

In other fields, the problem of visual servo control to grasp a moving object has received some attention. Allen et al. (1993) designed a visual servo controller based on trajectory parameterization using observed target positions. Kalman filter based motion estimators integrated with visual servo controllers have been used in object tracking and grasping in Fagerer et al. (1994), Janabi-Sharifi and Wilson (1998), and Nomura and Naito (2000). Off-line training based Horaud et al. (1998) and online model-based Kragić et al. (2001) trajectory planners are developed for autonomous object grasping. Image-based visual servo controller with rule-based gain scheduling is proposed in Wang et al. (2014). The problem of vision-based landing of an unmanned aerial vehicle on a moving platform is considered in Herisse et al. (2010) and Serra et al. (2014). Adaptive visual servo controllers are presented in Smith and Papanikolopoulos (1997), Mehta et al. (2011, 2015) that employ online parameter update laws to identify the unknown target motion. Although successful in their research endeavors, most of the controllers above have limitations to robotic harvesting system. The stability of the controllers in Allen et al. (1993), Fagerer et al. (1994), Nomura and Naito (2000), and Wang et al. (2014) cannot be guaranteed, and hence performance in terms of harvesting efficiency and cycle time cannot be assured. Another challenge in robotic fruit harvesting is to consistently obtain robust feature points of a fruit that can be tracked between camera image frames. Therefore, controllers Janabi-Sharifi and Wilson (1998), Smith and Papanikolopoulos (1997), Kragić et al. (2001), Herisse et al. (2010), and Serra et al. (2014) that rely on tracked feature points or optical flow may not be suitable for fruit harvesting. Our prior work in Mehta et al. (2015) considered an adaptive visual servo controller for a missile to intercept a moving target. Although the controller does not require multiple tracked feature points, it assumes linearly parameterizable and continuous in time disturbance dynamics.

The contribution of this paper is in the development of a nonlinear robust visual servo controller for robotic fruit harvesting in the presence of unknown fruit motion. The presented work, building on our preliminary results in Mehta et al. (2014), differs from the existing approaches in that the disturbance dynamics are included in control formulation to actively compensate for the fruit motion without high-gain or high-frequency image feedback. Specifically, robust feedback elements that upper bound the unknown nonlinear disturbances are used in the control laws. Apart from boundedness, the controller does not assume any knowledge or structure of the disturbance. Also, the presented controller does not rely on feature point tracking and only requires the knowledge of the fruit centroid position in the image frame, which makes it more suitable for the unstructured grove environments. In contrast to Mehta et al. (2014), uncertainties in the fruit motion are also considered in designing rotation controller to ensure that the CIH can view the target fruit. Finally, Lyapunov-based stability analysis is presented to guarantee uniformly ultimately bounded regulation of an end-effector to the target fruit. In other words, the proposed controller ensures that the end-effector can be driven arbitrarily close to the fruit in finite time and remains close to the fruit even in the presence of fruit motion. It will also be proved that by selecting appropriate control gains the desired pick cycle time or fruit removal rate can be achieved. To the best knowledge of the authors, the presented work is the first to provide robust nonlinear control formulation with detailed stability and performance analysis for robotic fruit harvesting. The developed controller is verified using extensive numerical simulations for varying levels of fruit displacement $\{35, 70, 105, 140, 175, 210\}$ mm. In addition, the performance the developed controller is evaluated in indoor proof-of-concept experiments using Robotics Research K1607 7-DOF kinematically redundant manipulator for 120 mm fruit displacement. The performance of the developed robust controller is compared with a feedback controller without robustifying terms. The results demonstrate stable closed-loop operation with disturbance rejection using the developed robust controller and does not show oscillatory behavior exhibited by the non-robust controller. Although focused on citrus harvesting, the general control architecture is suitable for any fruit and vegetable with general spherical or ellipsoidal geometry, such as apples and tomatoes.

The presented paper is organized as follows: Section 2 introduces the fruit localization geometry; Section 3 states the control objective; robust rotation and translation controllers are developed in Section 4; the stability analysis presented in Section 5; the finite-time convergence analysis and its impact on pick cycle time is presented in 6. Simulation results are presented in Section 7 while Section 8 provides experimental evidence. Nomenclature is provided in Appendix A, and Appendix B discusses various challenges pertaining to field operation in relation to the developed controller.

2. Euclidean reconstruction

A cooperative camera scheme consisting of a fixed camera and a CIH are considered. The fixed camera, e.g., a stationary camera mounted in the robot workspace, can view an entire or part of a tree canopy. A global fruit map along with suitable harvesting sequence can be determined by the fixed camera. The objective is to servo the CIH held by an end-effector to the target fruit to be harvested from the global map. While servoing to the target fruit, the CIH can view fruits that are not present in the initial global map. The CIH has this advantage because it can view the canopy from orientations different from the stationary fixed camera. In addition, the CIH can obtain close-up images of fruits for improved positioning accuracy due to its proximity to canopy during harvesting.

Consider the orthogonal coordinate frames $\mathcal{F}, \mathcal{F}_f$, and $\mathcal{F}_b$ as shown in Fig. 1. The time-varying coordinate frame $\mathcal{F}$ is attached to a CIH. The fixed coordinate frames $\mathcal{F}_f$ and $\mathcal{F}_b$ are attached to a fixed camera and the stationary base joint of a robot, respectively. The unknown Euclidean coordinates of the fruit center, $\bar{m}(t), \bar{m}_f \in \mathbb{R}^3$, expressed in terms of $\mathcal{F}$ and $\mathcal{F}_f$, respectively, are given as

$$\bar{m}(t) \triangleq [x(t) \quad y(t) \quad z(t)]^T, \quad \bar{m}_f \triangleq [x_f \quad y_f \quad z_f]^T \tag{1}$$

where $z(t),\ z_f \in \mathbb{R}$ denote the unknown depth of the fruit measured in $\mathcal{F}$ and $\mathcal{F}_f$, respectively. The Euclidean-space is projected onto the image-space, and $m(t)$ and m_f denote the corresponding normalized Euclidean coordinates of the fruit center as

$$m(t) \triangleq \left[\frac{x(t)}{z(t)} \quad \frac{y(t)}{z(t)} \quad 1\right]^T, \quad m_f \triangleq \left[\frac{x_f}{z_f} \quad \frac{y_f}{z_f} \quad 1\right]^T. \tag{2}$$

Assumption 1. In (2), it is assumed that the unknown depths $z(t), z_f > \varepsilon$, where $\varepsilon \in \mathbb{R}_{>0}$ is a constant. This is a standard assumption in visual servo control, which physically means that the target is always in front of the camera. In practice, the parameter ε can be equal to or greater than the minimum focusing distance of the camera lens.

In addition to having normalized task-space coordinates, the fruit center will also have pixel coordinates acquired by the CIH and the fixed camera. Let $p(t), p_f \in \mathbb{R}^2$ denote the pixel coordinates of the fruit center expressed in $\mathcal{F}$ and $\mathcal{F}_f$, respectively, as

$$p(t) \triangleq [u(t) \quad v(t)]^T, \quad p_f \triangleq [u_f \quad v_f]^T. \tag{3}$$

Since the normalized Euclidean coordinates in (2) cannot be measured directly, a global invertible transformation (i.e., the pinhole camera model) is used to determine the normalized Euclidean coordinates from the corresponding pixel information as

$$\left[p^T \quad 1\right]^T = Am, \quad \left[p_f^T \quad 1\right]^T = A_f m_f. \tag{4}$$

In (4), $A, A_f \in \mathbb{R}^{3\times 3}$ denote the known constant invertible intrinsic camera calibration matrices for the CIH and the fixed camera, respectively.

Leveraging on our efforts in Mehta and Burks (2014b), the depth of a fruit can be estimated via perspective transformation by assuming known geometry of the fruit variety as[1]

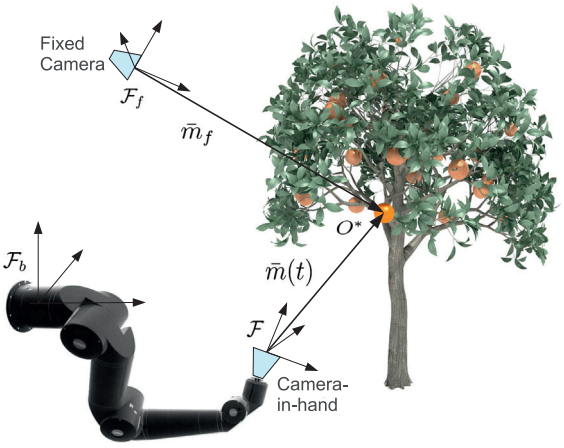

Fig. 1. Coordinate frame relationships, where the time-varying frame $\mathcal{F}$ is attached to the camera-in-hand, $\mathcal{F}_f$ corresponds to the fixed camera, and $\mathcal{F}_b$ is attached to the stationary base of the robot.

$$\hat{z}_f = \frac{f_f(\lambda_{xf} d_{ox} d_{iy} + \lambda_{yf} d_{oy} d_{ix})}{2 d_{ix} d_{iy}} \tag{5}$$

$$d_{ix} = 2\left(\frac{A_p}{\pi\sqrt{1-\tilde{e}^2}}\right)^{1/2} \quad d_{iy} = 2\left(\frac{A_p\sqrt{1-\tilde{e}^2}}{\pi}\right)^{1/2} \tag{6}$$

where $\hat{z}_f \in \mathbb{R}$ denotes the estimated Euclidean depth of a fruit measured in $\mathcal{F}_f$; $d_{ox}, d_{oy} \in \mathbb{R}$ denote the sample mean major and minor axes, respectively, of an ellipsoidal fruit; $d_{ix}, d_{iy} \in \mathbb{R}$ denote the major and minor axes, respectively, in the image plane; $A_p \in \mathbb{R}$ denotes the area of the fruit in the image plane of the fixed camera (in pixels); $\tilde{e} \in \mathbb{R}$ is the known eccentricity of the ellipse; the constant $f_f \in \mathbb{R}_{>0}$ represents the focal length in pixels for the fixed camera; and $\lambda_{xf}, \lambda_{yf} \in \mathbb{R}_{>0}$ are the scaling factors in the image x and y directions of the fixed camera, respectively.

Remark 1. Any inaccuracy in estimating the fruit size A_p affects the major and minor axes, d_{ix} and d_{iy}, respectively. As stated in Remark 1 in Mehta and Burks (2014b), it can be shown that d_{ix}/d_{iy} is constant and hence the unknown depth ratio $\hat{z}_f/z_f$, denoted by $\gamma_z \in \mathbb{R}_{>0}$, is also constant. The effect of depth uncertainty on the controller performance is thoroughly analyzed in Appendix B.1 of the presented paper.

3. Control objective

The goal is to locate the CIH coordinate frame to the target fruit position in the presence of unknown fruit motion, which can be achieved by regulating the time-varying fruit image coordinates $p(t)$ to the desired image coordinates, and driving the end-effector to the desired fruit depth. Hence, mathematically, the control objective can be stated as

$$p(t) \to p_d, \quad p_d = [u_0 \quad v_0]^T \quad \text{and} \quad z(t) \leqslant z_d \tag{7}$$

where $z_d \in \mathbb{R}_{>0}$ denotes the maximum desired depth of the fruit in $\mathcal{F}$, and $u_0, v_0 \in \mathbb{R}$ denote the pixel coordinates of the principal point (i.e., the intersection of an optical axis with the image plane) of the CIH.

To control the position and orientation of $\mathcal{F}$, a relationship is required to relate the linear and angular camera velocities to the linear and angular velocities of the robot (i.e., the actual kinematic control inputs) that enables an on-board camera motion. This

[1] The depth estimator in (5) assumes complete visibility of the fruit. In the presence of partial occlusions or clustered fruit, advanced methods such as perimeter detection and shape analysis techniques Plebe and Grasso (2001) and Hannan et al. (2009) can be used to directly obtain the image-space diameters d_{ix}, d_{iy} of the fruit to get $\hat{z}_f$ using (5).

relationship is dependent on the extrinsic calibration parameters as (Malis and Chaumette, 2002)

$$\begin{bmatrix} v_c \\ \omega_c \end{bmatrix} = \begin{bmatrix} R_e & [t_e]_\times R_e \\ \mathbf{0} & R_e \end{bmatrix} \begin{bmatrix} v_r \\ \omega_r \end{bmatrix} \tag{8}$$

where $v_c(t), \omega_c(t) \in \mathbb{R}^3$ denote the linear and angular velocity of the camera; $v_r(t), \omega_r(t) \in \mathbb{R}^3$denote the linear and angular velocity of the robot; $R_e \in \mathbb{R}^{3\times3}$ denotes the constant rotation between the CIH and the robot end-effector frames; $[t_e]_\times \in \mathbb{R}^{3\times3}$ is a skew symmetric matrix of $t_e \in \mathbb{R}^3$, which denotes the constant translation vector between the CIH and robot frames; and $\mathbf{0} \in \mathbb{R}^{3\times3}$ is a zero matrix.

4. Control development

As discussed earlier, the fixed camera can view an entire or part of a tree canopy. Using (5) and (6), the fixed camera can obtain a global fruit map and the corresponding harvesting sequence such as in Edan et al. (1991). However, the fruit to be harvested from the sequence may not be visible to the CIH, say, because the CIH is pointing away from the fruit. Therefore, a nonlinear rotation controller is developed to orient the CIH such that the target fruit enters its field-of-view (FOV). The rotation controller uses the estimated fruit position obtained by the fixed camera to determine the desired orientation of the CIH. Once the target fruit is visible to the CIH, the translation controller regulates the end-effector to the target fruit using image feedback from the CIH. The developed rotation and translation controllers assume unknown non-vanishing bounded disturbances.

4.1. Rotation controller

In this section, a controller is developed to orient the robot end-effector such that the target fruit enters the FOV of the CIH. Using (2), (5), and (6), let the estimated Euclidean position of the fruit in the fixed camera $\mathcal{F}_f$ be denoted by $\hat{\bar{m}}_f \in \mathbb{R}^3$. The Euclidean coordinates $\hat{\bar{m}}_f$ can be expressed in the CIH as $\hat{\bar{m}}'(t)$ (see (9) and (12) in Mehta and Burks (2014b)). Therefore, the objective is to align $\hat{\bar{m}}'(t)$ along the direction of the camera's optical axis $[0 \quad 0 \quad 1]^T$.

The rotation error $e_\omega(t) \in \mathbb{R}^3$, which is defined as the orientation mismatch that brings the target fruit into the FOV of the CIH, can be expressed in angle–axis representation as

$$e_\omega \triangleq u\theta \tag{9}$$

where $u(t) \in \mathbb{R}^3$ represents a unit axis of rotation such that $u(t) = \vec{\hat{\bar{m}}}'(t) \wedge [0 \quad 0 \quad 1]^T$, and $\theta(t) = \cos^{-1}\langle \vec{\hat{\bar{m}}}'(t), [0 \quad 0 \quad 1]^T \rangle$. In (9), $\theta(t) \in \mathbb{R}, 0 \leqslant \theta(t) \leqslant \pi$ is the angle of rotation about $u(t)$ that brings $\hat{\bar{m}}'(t)$ along the optical axis of the CIH, and $\vec{\hat{\bar{m}}}'(t) \in \mathbb{R}^3$ is the time-varying unit vector along the estimated fruit position $\hat{\bar{m}}'(t)$.

The rotation error in (9) depends on the camera motion as well as the unknown fruit motion. Therefore, the open-loop error system obtained by taking the time-derivative of (9) contains two terms as

$$\dot{e}_\omega = L_\omega \omega_c + d_\omega \tag{10}$$

where $L_\omega(t) \in \mathbb{R}^{3\times3}$ is defined as (Malis and Chaumette, 2002)

$$L_\omega = I_3 - \frac{\theta}{2}[u]_\times + \left(1 - \frac{\operatorname{sinc}(\theta)}{\operatorname{sinc}^2\left(\frac{\theta}{2}\right)}\right)[u]_\times^2 \tag{11}$$

and $d_\omega \in \mathbb{R}^3$ is the exogenous disturbance as a result of fruit motion. The disturbance is assumed to be bounded such that $\|d_\omega\| \leqslant \gamma_\omega$, where $\gamma_\omega \in \mathbb{R}_{>0}$ and $\|\cdot\|$ denotes the L^2 vector norm. In (11), the $\operatorname{sinc}(\theta)$ term denotes the unnormalized sinc function, $[u]_\times$ is the skew-symmetric matrix of $u(t)$, and I_3 denotes a 3×3 identity matrix. The determinant of $L_\omega(t)$ is $\det(L_\omega) = 1/\operatorname{sinc}^2(\theta/2)$, thus being singular only at $\theta = 2k\pi \; \forall k \in \mathbb{N}_{>0}$, i.e., outside of $0 \leqslant \theta(t) \leqslant \pi$. Based on the open-loop error dynamics in (10) and the subsequent stability analysis, the angular velocity of the camera can be designed as

$$\omega_c = -k_\omega e_\omega - \frac{e_\omega \gamma_\omega^2}{\|e_\omega\|\gamma_\omega + \epsilon_\omega} \tag{12}$$

where $k_\omega \in \mathbb{R}_{>0}$ is the control gain, and $\epsilon_\omega \in \mathbb{R}_{>0}$ is chosen to be arbitrarily small. The closed-loop error system can be obtained after substituting (12) in (10) as

$$\dot{e}_\omega = -k_\omega L_\omega e_\omega + -\frac{L_\omega e_\omega \gamma_\omega^2}{\|e_\omega\|\gamma_\omega + \epsilon_\omega} + d_\omega. \tag{13}$$

4.2. Translation controller

Taking the time derivative of (4), the velocity of the CIH can be related to the image-space velocity $\dot{p}(t) \in \mathbb{R}^2$ of the fruit centroid $p(t)$ as

$$\dot{p} = \begin{bmatrix} \dot{u} \\ \dot{v} \end{bmatrix} = -\frac{1}{z} J_v v_c - J_\omega \omega_c + d_p. \tag{14}$$

In (14), $J_v(u, v), J_\omega(u, v) \in \mathbb{R}^{2\times3}$ are measurable image Jacobians that relate the linear and angular velocity, respectively, of the CIH to the fruit image velocity, and $d_p(t) \in \mathbb{R}^2$ is the unknown fruit motion in the image plane due to exogenous disturbances acting on the fruit. The disturbance $d_p(t)$ in (14) satisfies $\|d_p(t)\| \leqslant \gamma_p$, where $\gamma_p \in \mathbb{R}_{>0}$ is a known bounding constant. The constant γ_p can be chosen to upper bound the image-space velocity of the fruit due to disturbance alone.

The translation controller will provide necessary linear actuation to reject disturbances and maintain the fruit in the FOV. Since no orientation change is required during translation control, the image dynamics can be obtained by substituting $\omega_c(t) = 0$ in (14) as

$$\dot{p} = -\frac{1}{z} J_v' v_c' - \frac{1}{z} J_v'' v_{cz} + d_p \tag{15}$$

where $v_{cz}(t) \in \mathbb{R}$ is the control velocity along the optical axis of the CIH, the measurable Jacobians $J_v' \in \mathbb{R}^{2\times2}$ and $J_v''(u, v) \in \mathbb{R}^2$ and the control velocity in the image plane $v_c'(t) \in \mathbb{R}^2$ are defined as

$$J_v' = \begin{bmatrix} \lambda_x f & 0 \\ 0 & \lambda_y f \end{bmatrix} \quad J_v'' = -\begin{bmatrix} u - u_0 \\ v - v_0 \end{bmatrix} \quad v_c' = \begin{bmatrix} v_{cx} \\ v_{cy} \end{bmatrix}. \tag{16}$$

Based on the control objective in (7), the translation error $e_v(t) = \left[e_{v1}^T(t) \; e_{v2}(t)\right]^T \in \mathbb{R}^3$ can be defined as

$$e_{v1} \triangleq p - p_d \tag{17}$$

$$e_{v2} \triangleq \alpha\hat{z} - z_d \tag{18}$$

where $\alpha \in \mathbb{R}_{>0}$ is a constant that ensures $\alpha\hat{z} \geqslant z$. The time-varying estimated fruit depth $\hat{z}(t)$ in $\mathcal{F}$ can be obtained by obtaining expressions similar to (5) and (6) when the target fruit is visible to the CIH. The constant α in (18) can be selected arbitrarily large to ensure the robot reaches the target fruit despite any depth estimation errors. Since $z \leqslant \alpha\hat{z}$, the robot may overshoot the target fruit, and hence the end-effector is equipped with an infrared proximity sensor to stop once the fruit is reached.

Assuming the estimated fruit depth $\hat{z}(t)$ to be a continuous function of time, the open-loop error dynamics can be obtained by taking the time-derivative of (18) as

$$\dot{e}_{v2} = -\alpha\xi v_{cz} + d_z \tag{19}$$

where $d_z(t) \in \mathbb{R}$ is the component of fruit motion along the optical axis, such that $|d_z(t)| \leqslant \gamma_d$ for $\gamma_d \in \mathbb{R}_{>0}$, and ξ denotes the constant depth ratio $\hat{z}/z$. γ_d indicates an upper bound on the fruit velocity along the optical axis due to disturbance. Based on (19), the linear velocity $v_{cz}(t)$ of the CIH along the optical axis can be designed as

$$v_{cz} = k_z e_{v2} + \frac{e_{v2}\gamma_d^2}{|e_{v2}|\gamma_d + \epsilon_z} - w\|e_{v1}\|^2 \tag{20}$$

where $k_z = k_{z1} + k_{z2} \in \mathbb{R}_{>0}$ is the constant control gain, $\epsilon_z \in \mathbb{R}_{>0}$ is an arbitrarily small design constant, and $w \in \mathbb{R}_{>0}$ is the user defined weight on the term $\|e_{v1}\|^2$. The control gain k_z determines response of the controller to the input error $e_{v2}(t)$, however, large gains should be avoided in the presence of measurement noise. Substituting (20) into (19), the closed-loop error system can be obtained as

$$\dot{e}_{v2} = -\alpha\xi k_z e_{v2} - \frac{\alpha\xi e_{v2}\gamma_d^2}{|e_{v2}|\gamma_d + \epsilon_z} + d_z + \alpha\xi w\|e_{v1}\|^2. \tag{21}$$

Remark 2. From the definitions of α and ξ, the product $\alpha\xi \geqslant 1$. Therefore, the closed-loop system in (21) can be considered to be subjected to an additive disturbance $\alpha\xi w\|e_{v1}\|^2$. The disturbance term $\alpha\xi w\|e_{v1}\|^2$ guarantees that the target fruit is centered in the FOV of the CIH (or the end-effector) before reaching the fruit.

To design control input $v_c'(t)$, an open-loop error system can be obtained by taking the time-derivative of (17) and substituting (15) into the resulting expression as

$$\dot{e}_{v1} = -\frac{1}{z}J_v' v_c' - \frac{1}{z}J_v'' v_{cz} + d_p. \tag{22}$$

Based on the open-loop error system in (22) and the subsequent stability analysis, the linear control velocity $v_c'(t) \in \mathbb{R}^2$ of the CIH can be designed as

$$v_c'(t) = J_v'^{-1}\left(\alpha\hat{z}k_p e_{v1} - J_v'' v_{cz} + \frac{\alpha\hat{z}e_{v1}\gamma_p^2}{\|e_{v1}\|\gamma_p + \epsilon_p}\right) \tag{23}$$

where $k_p \in \mathbb{R}_{>0}$ is the constant control gain, and $\epsilon_p \in \mathbb{R}_{>0}$ is an arbitrarily small design constant. Similar to k_z, the control gain k_p determines response of the controller to input error $e_{v1}(t)$. After substituting the control input in (23) into (22), and using the fact that $\hat{z}/z = \xi$, the closed-loop error system can be obtained as

$$\dot{e}_{v1} = -\alpha\xi k_p e_{v1} - \frac{\alpha\xi e_{v1}\gamma_p^2}{\|e_{v1}\|\gamma_p + \epsilon_p} + d_p. \tag{24}$$

Substituting (12), (20), and (23) in (8) and using the fact that $v_c = [v_c'^T \; v_{cz}]^T$, the desired angular and linear velocity of the robot end-effector can be obtained.

5. Stability analysis

Theorem 1. *The rotation controller orients the end-effector such that the target fruit appears arbitrarily close to the center of the CIH. Formally, the rotation control input developed in (12) ensures uniformly ultimately bounded regulation of the end-effector in the sense that*

$$\|e_\omega(t)\| \leqslant \zeta_0 \exp\{-\zeta_1 t\} + \zeta_2 \tag{25}$$

where ζ_0, ζ_1, and $\zeta_2 \in \mathbb{R}$ denote positive bounding constants.

Proof. Let $V_1(t)$ be the following nonnegative Lyapunov candidate function:

$$V_1 = \frac{1}{2}e_\omega^T e_\omega \tag{26}$$

$$\lambda_1\|e_\omega\|^2 \leqslant V_1 \leqslant \lambda_2\|e_\omega\|^2 \tag{27}$$

where $\lambda_1, \lambda_2 \in \mathbb{R}_{>0}$ are known bounding constants. Taking the time-derivative of $V_1(t)$ and using (13), the upper bound on the Lyapunov derivative can be obtained as

$$\dot{V}_1 \leqslant -k_\omega\|e_\omega\|^2 - \frac{\|e_\omega\|^2\gamma_\omega^2}{\|e_\omega\|\gamma_\omega + \epsilon_\omega} + \|e_\omega\|\gamma_\omega \tag{28}$$

where the property $L_\omega e_\omega = e_\omega$ along with the fact $\|d_\omega\| \leqslant \gamma_\omega$ are used. The expression in (28) can be simplified as

$$\dot{V}_1 \leqslant -k_\omega\|e_\omega\|^2 + \epsilon_\omega. \tag{29}$$

Consequently, (27) can be used to obtain the inequality

$$\dot{V}_1 \leqslant -\frac{k_\omega}{\lambda_2}V_1 + \epsilon_\omega. \tag{30}$$

The linear differential inequality in (30) can be solved as

$$V_1 \leqslant V_1(0)\exp\left\{\frac{-k_\omega}{\lambda_2}(t-t_0)\right\} + \frac{\epsilon_\omega\lambda_2}{k_\omega}\left(1 - \exp\left\{\frac{-k_\omega}{\lambda_2}(t-t_0)\right\}\right). \tag{31}$$

The expressions in (26), (27), and (30) can be used to conclude that $e_\omega(t) \in \mathcal{L}_\infty$. Since $d_\omega(t) \in \mathcal{L}_\infty$, (13) can be used to conclude that $\dot{e}_\omega(t) \in \mathcal{L}_\infty$. The inequalities in (27) and (31) can be used to conclude that

$$\|e_\omega(t)\| \leqslant \left(\frac{\lambda_2\|e_\omega(0)\|^2}{\lambda_1} - \frac{\epsilon_\omega\lambda_2}{k_\omega\lambda_1}\right)^{1/2}\exp\left\{\frac{-k_\omega}{2\lambda_2}(t-t_0)\right\} + \left(\frac{\epsilon_\omega\lambda_2}{k_\omega\lambda_1}\right)^{1/2}. \tag{32}$$

The result in (25) can be directly obtained from (32). It can be seen from (32) that as

$$\lim_{t\to\infty}\|e_\omega(t)\| \leqslant \left(\frac{\epsilon_\omega\lambda_2}{k_\omega\lambda_1}\right)^{1/2} = e_{\omega\infty}. \tag{33}$$

Hence, the manipulator can be oriented along the direction of the target fruit in the presence of unknown fruit motion, where the size of the error ball $e_{\omega\infty}$ can be reduced by arbitrarily reducing ϵ_ω. □

Theorem 2. *The translation controller guarantees that the end-effector is placed arbitrarily close to the target fruit location. Formally, the translation control inputs developed in (20) and (23) ensure uniformly ultimately bounded regulation of the end-effector in the sense that*

$$\|e_{v1}(t)\| \leqslant \zeta_3\exp\{-\zeta_4 t\} + \zeta_5 \tag{34}$$

$$\|e_{v2}(t)\| \leqslant \zeta_6\exp\{-\zeta_7 t\} + \zeta_8 \tag{35}$$

where $\zeta_3, \zeta_4, \zeta_5, \zeta_6, \zeta_7, \zeta_8 \in \mathbb{R}$ denote positive bounding constants.

Proof. Let $V_2(t)$ be the following nonnegative function:

$$V_2 = \frac{1}{2}e_{v1}^T e_{v1} \tag{36}$$

$$\lambda_3\|e_{v1}\|^2 \leqslant V_2 \leqslant \lambda_4\|e_{v1}\|^2 \tag{37}$$

where $\lambda_3, \lambda_4 \in \mathbb{R}_{>0}$ are known bounding constants. Taking the time-derivative of $V_2(t)$ and using (24), the upper bound on the Lyapunov derivative can be obtained as

$$\dot{V}_2 \leqslant -\alpha\xi k_p\|e_{v1}\|^2 - \frac{\alpha\xi\|e_{v1}\|^2\gamma_p^2}{\|e_{v1}\|\gamma_p + \epsilon_p} + \|e_{v1}\|\gamma_p \tag{38}$$

where the fact that $\|d_p(t)\| \leqslant \gamma_p$ is used. Using the fact that $\alpha\xi \geqslant 1$, the expression in (38) can be simplified as

$$\dot{V}_2 \leqslant -\alpha\xi k_p \|e_{v1}\|^2 + \epsilon_p. \tag{39}$$

The expressions in (36), (37), and (39) can be used to conclude that $e_{v1}(t) \in \mathcal{L}_\infty$. Since $d_p(t) \in \mathcal{L}_\infty$, (24) can be used to conclude that $\dot{e}_{v1}(t) \in \mathcal{L}_\infty$. Following the procedure in Theorem (1), the bound on the error $e_{v1}(t)$ can be obtained as

$$\|e_{v1}(t)\| \leqslant \left(\frac{\lambda_4\|e_{v1}(0)\|^2}{\lambda_3} - \frac{\epsilon_p\lambda_4}{\alpha\xi k_p\lambda_3}\right)^{1/2} \exp\left\{\frac{-\alpha\xi k_p}{2\lambda_4}(t-t_0)\right\} + \left(\frac{\epsilon_p\lambda_4}{\alpha\xi k_p\lambda_3}\right)^{1/2}. \tag{40}$$

The result in (34) can now be directly obtained from (40). From (40), it can be seen that

$$\lim_{t\to\infty} \|e_{v1}(t)\| \leqslant \left(\frac{\epsilon_p\lambda_4}{\alpha\xi k_p\lambda_3}\right)^{1/2} = e_{v1\infty}. \tag{41}$$

Hence, the image coordinates of the fruit centroid are regulated within a ball of radius $e_{v1\infty}$ centered at p_d, where the size of the error ball can be reduced by arbitrarily reducing ϵ_p.

Using the result in (34), the disturbance term $\alpha\xi w\|e_{v1}\|^2$ in (21) can be upper bounded as $\alpha\xi w\|e_{v1}\|^2 \leqslant \alpha\xi w(\zeta_3' + \zeta_5')$ for $\zeta_3', \zeta_5' \in \mathbb{R}_{>0}$. To analyze the stability of the closed-loop system in (21), consider a nonnegative function $V_2(t)$ as

$$V_3 = \frac{1}{2}e_{v2}^2 \tag{42}$$

$$\lambda_5 e_{v2}^2 \leqslant V_3 \leqslant \lambda_6 e_{v2}^2 \tag{43}$$

where $\lambda_5, \lambda_6 \in \mathbb{R}_{>0}$ are known bounding constants. Using (21) and (34), the time-derivative of $V_3(t)$ can be upper bounded as

$$\dot{V}_3 \leqslant -\alpha\xi k_z |e_{v2}|^2 + \alpha\xi w(\zeta_3' + \zeta_5')|e_{v2}| + \epsilon_z \tag{44}$$

where the facts that $\alpha\xi \geqslant 1$ and $|d_z(t)| \leqslant \gamma_d$ are used. Completing the squares and using (43) yields the following inequality:

$$\dot{V}_3 \leqslant \frac{-\alpha\xi k_{z1}}{\lambda_6} V_3 + \frac{\alpha\xi w^2(\zeta_3' + \zeta_5')^2}{4k_{z2}} + \epsilon_z \tag{45}$$

where $k_z = k_{z1} + k_{z2}$ is used. Standard signal chasing arguments as presented in Theorem 1 can be applied to guarantee boundedness of the states and control inputs. Further, the inequalities in (43) and (45) can be used to conclude that

$$|e_{v2}(t)| \leqslant \left(\frac{\lambda_6|e_{v2}(0)^2|}{\lambda_5} - \frac{\lambda_6}{\alpha\xi k_{z1}\lambda_5}\left(\frac{\alpha\xi w^2(\zeta_3' + \zeta_5')^2}{4k_{z2}} + \epsilon_z\right)\right)^{1/2} \times \exp\left\{\frac{-\alpha\xi k_{z1}}{2\lambda_6}(t-t_0)\right\} + \left(\frac{\lambda_6}{\alpha\xi k_{z1}\lambda_5}\left(\frac{\alpha\xi w^2(\zeta_3' + \zeta_5')^2}{4k_{z2}} + \epsilon_z\right)\right)^{1/2} \tag{46}$$

The result in (35) follows directly from (46). In the limit $t \to \infty$, the bound on the error can be obtained as

$$\lim_{t\to\infty} |e_{v2}(t)| \leqslant \left(\frac{\lambda_6}{\alpha\xi k_{z1}\lambda_5}\left(\frac{\alpha\xi w^2(\zeta_3' + \zeta_5')^2}{4k_{z2}} + \epsilon_z\right)\right)^{1/2} = e_{v2\infty}. \tag{47}$$

The translation error $e_{v2}(t)$ along the camera optical axis can be reduced by arbitrarily reducing ϵ_p and ϵ_z, hence the end-effector is regulated to the fruit such that $z(t) \leqslant z_d$. An infrared proximity switch on the end-effector can detect the presence of fruit to stop the manipulator to ensure $\epsilon \leqslant z(t) \leqslant z_d$.

6. Impact of finite-time convergence on harvesting time

From (45) and (47), it can be seen that $\dot{V}_3 < 0$ if the following inequality is satisfied:

$$|e_{v2}| > \delta, \quad \text{where} \quad \delta = \left(\frac{w^2(\zeta_3' + \zeta_5')^2\lambda_6}{4k_{z1}k_{z2}\lambda_5} + \frac{\epsilon_z\lambda_6}{\alpha\xi k_{z1}\lambda_5}\right)^{\frac{1}{2}}. \tag{48}$$

In other words, $\dot{V}_3 < 0$ for all $e_{v2}(t)$ outside the compact set $B_\delta = \{|e_{v2}| \leqslant \delta\}$ in Fig. 2. For the Lyapunov candidate function in (42), let $\delta^2/2 < b < c$. Consider a compact set $\Omega_c = \{V_3 \leqslant c | e_{v2} \in B_c\}$, where $B_c = \{|e_{v2}| \leqslant \sqrt{2c}\}$. All the system trajectories starting in Ω_c will remain in this set for all future times since $\dot{V}_3 < 0$ on the boundary of Ω_c.

Consider another compact set $\Omega_b = \{V_3 \leqslant b | e_{v2} \in B_b\}$, where $B_b = \{|e_{v2}| \leqslant \sqrt{2b}\}$. Ω_c and Ω_b are positively invariant sets since $\dot{V}_3 < 0,\ \forall |e_{v2}| > \delta$. Let $\Gamma = \{b \leqslant V_3 \leqslant c\}$ be a compact set. From (45) and the fact that $\delta^2/2 < b < c$,

$$\dot{V}_3 < \frac{-\alpha\xi k_{z1}}{\lambda_6} V_3, \qquad \forall e_{v2}(t) | V_3(e_{v2}) \in \Gamma, \quad \forall t \geqslant t_0 \tag{49}$$

so that

$$V_3(e_{v2}(t)) < V_3(e_{v2}(0)) \exp\left\{\frac{-\alpha\xi k_{z1}(t-t_0)}{\lambda_6}\right\}. \tag{50}$$

From (50), it is clear that any system trajectory for which $V_3(e_{v2}(0)) \in \Gamma$ enters the set B_b in finite time, and remains in this set for all future times. The maximum time $t_{e_{v2}}$ for the system trajectory to enter B_b can be obtained from (50) as

$$t_{e_{v2}} < t_0 + \frac{\lambda_6(\log(c) - \log(b))}{\alpha\xi k_{z1}}. \tag{51}$$

Similar analysis can be used to prove that the image error $e_{v1}(t)$ converges to a ball $B_d = \left\{|e_{v1}| \leqslant \sqrt{2d}\right\}$ from $B_e = \left\{|e_{v1}| \leqslant \sqrt{2e}\right\}$ for any $\mathbb{R}_{>0} < d < e$ in maximum time $t_{e_{v1}}$. Also, the maximum time t_{e_ω} required for the angular error $e_\omega(t)$ to converge to a ball $B_f = \left\{|e_\omega| \leqslant \sqrt{2f}\right\}$ from $B_g = \left\{|e_\omega| \leqslant \sqrt{2g}\right\}$ for any $\mathbb{R}_{>0} < f < g$ can be obtained.

From the harvesting point of view, the radius of the balls B_b and B_d can be defined as the maximum allowable deviation of the end-effector from the target fruit that can still result in successful fruit harvesting. The goal of rotation control is to bring a target fruit in the CIH's FOV, and not necessarily along the optical axis of the camera. Therefore, large rotation errors can be tolerated, and the radius of the ball B_f can be selected large. It is clear from the controller design in (20) that the robot regulates to the desired depth only after the image error becomes arbitrarily small, and hence $t_{e_{v1}} < t_{e_{v2}}$. Using the above analysis, the maximum time to servo the end-effector to this region of allowable deviation is $t_{e_\omega} + t_{e_{v2}}$. From (51), the control gain k_{z1} can be increased to reduce the time $t_{e_{v2}}$ to reach

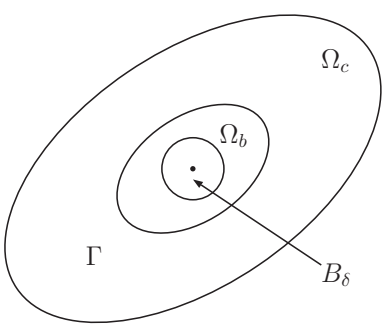

Fig. 2. Finite-time analysis of the solution.

the allowable set, and similarly the gain k_ω can be increased to reduce t_{e_ω}. Due to positive invariance, once entered, the end-effector never leaves the allowable set. Therefore, based on the size of B_b and B_f, the maximum pick cycle time can be obtained for the given control gains. Alternately, from (51), it is clear that the control gains k_{z1} and k_ω can be selected to achieve the desired maximum cycle time. In addition, increasing the control gains k_ω, k_{z1}, and k_{z1} reduces the ultimate bound on the regulation errors given in (33) and (47), and as such, the radius of balls B_b and B_f can be reduced for improved accuracy. However, as with any control practice, dynamic limitations and actuator constraints of the manipulator should be kept in mind when selecting high control gains.

Remark 3. The robust controller developed in this paper does not rely on the knowledge of the fruit motion. It can be seen from (12), (20), and (20) that only the upper bound on the disturbance is assumed to be known. Further, it is evident from the finite time analysis that the maximum cycle time depends only on the initial errors, $e_\omega(0)$ and $e_{v2}(0)$, and the choice of $B_b, B_f, k_\omega, k_{z1}$. For the given fruit motion, given the initial errors the maximum cycle time can be obtained. Therefore, the fruit motion does not directly influence the cycle time.

Remark 4. The maximum cycle time does not explicitly depend on the uncertainty in the fruit position which can be due to uncertain depth estimation. Let $\hat{e}_\omega(0)$ and $\hat{e}_{v2}(0)$ be the initial rotation and translation errors, respectively, based on the true fruit position, and let $\hat{t}_{e_\omega}$ and $\hat{t}_{e_{v2}}$ be the corresponding convergence times. As a result of depth uncertainty, $|\hat{e}_\omega(0)|$ can be greater than $|e_\omega(0)|$. However, since the radius of the ball B_f can be selected large, the convergence time $\hat{t}_{e_\omega} \approx t_{e_\omega}$. The parameter α in (18) ensures that $|e_{v2}(0)| > |\hat{e}_{v2}(0)|$, and hence $t_{e_{v2}} > \hat{t}_{e_{v2}}$. Therefore, the cycle time $t_{e_\omega} + t_{e_{v2}}$ using the estimated fruit position can be considered as an upper bound to the actual cycle time.

7. Simulation results

A numerical simulation was performed to demonstrate the performance of the proposed robust controller. The initial position $t \in \mathbb{R}^3$ and orientation $R \in \mathbb{R}^{3\times3}$ of the robot end-effector with respect to $\mathcal{F}_b$ was considered to be

$$t = [20 \;\; 60 \;\; 500]^T, \;\; R = \begin{bmatrix} 0.4698 & -0.1955 & 0.8608 \\ 0.1710 & 0.9769 & 0.1285 \\ -0.8660 & 0.0868 & 0.4924 \end{bmatrix}, \tag{52}$$

and the position and orientation of the CIH frame $\mathcal{F}$ with respect to $\mathcal{F}_b$ was $t_r = [20 \;\; 60 \;\; 650]^T$ and $R_r = R$, respectively. The unperturbed position of the target fruit in $\mathcal{F}_b$ was considered to be $\bar{m}_b = [500 \;\; 400 \;\; 2500]^T$, and the estimated fruit position in $\mathcal{F}_b$ was assumed to be $\hat{\bar{m}}_b = [510 \;\; 392 \;\; 2650]^T$. A non-vanishing disturbance perturbed the fruit with a velocity of

$$d_v(t) = \frac{d}{dt}\left[r\cos(\theta_p)\sin(\theta_z) \;\; r\sin(\theta_p)\sin(\theta_z) \;\; -r\cos(\theta_z) \right]^T \tag{53}$$

$$\theta_p(t) = 10\cos(7t) \quad \theta_z(t) = 10\cos(7t) \tag{54}$$

where $r = \{100, 200, 300, 400, 500, 600\}$ causing the fruit centroid to displace by about $d_c = \{35, 70, 105, 140, 175, 210\}$ mm. The resulting fruit motion was unknown to the controller. In addition, the image coordinates of the fruit were assumed to be affected by a zero-mean Gaussian noise of standard deviation one pixel. The constants in (12), (20), and (23) were selected as

$$k_\omega = 0.5, \quad \gamma_\omega = 2, \quad \epsilon_\omega = 0.1, \tag{55}$$

$$k_p = 2, \quad k_z = 4, \quad \epsilon_p = 5, \quad \epsilon_z = 10, \tag{56}$$

$$\gamma_p = 25, \quad \gamma_d = 10, \quad \alpha = 1.1, \quad w = 0.5. \tag{57}$$

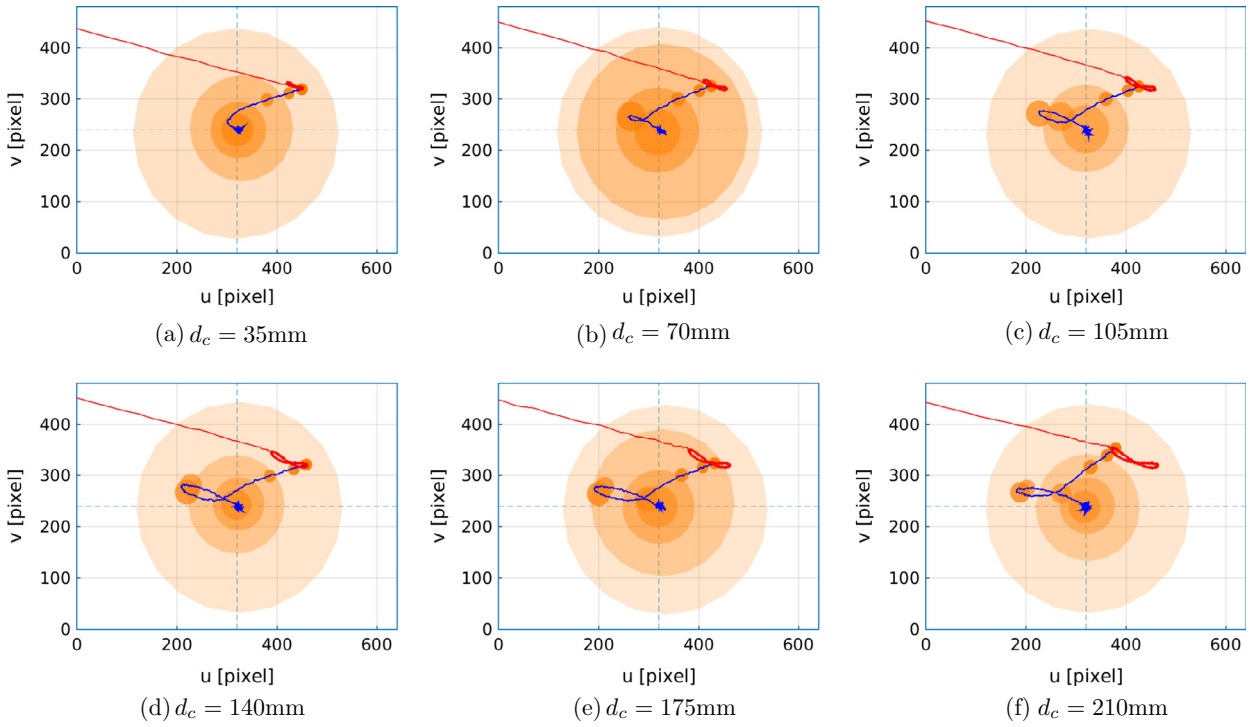

(a) $d_c = 35$mm (b) $d_c = 70$mm (c) $d_c = 105$mm

(d) $d_c = 140$mm (e) $d_c = 175$mm (f) $d_c = 210$mm

Fig. 3. Proposed robust controller: Time-varying fruit position and relative fruit size in the image plane of the camera-in-hand. The trajectories in red and blue refer to the observed fruit position during rotation and translation control, respectively. (For interpretation of the references to color in this figure legend, the reader is referred to the web version of this article.)

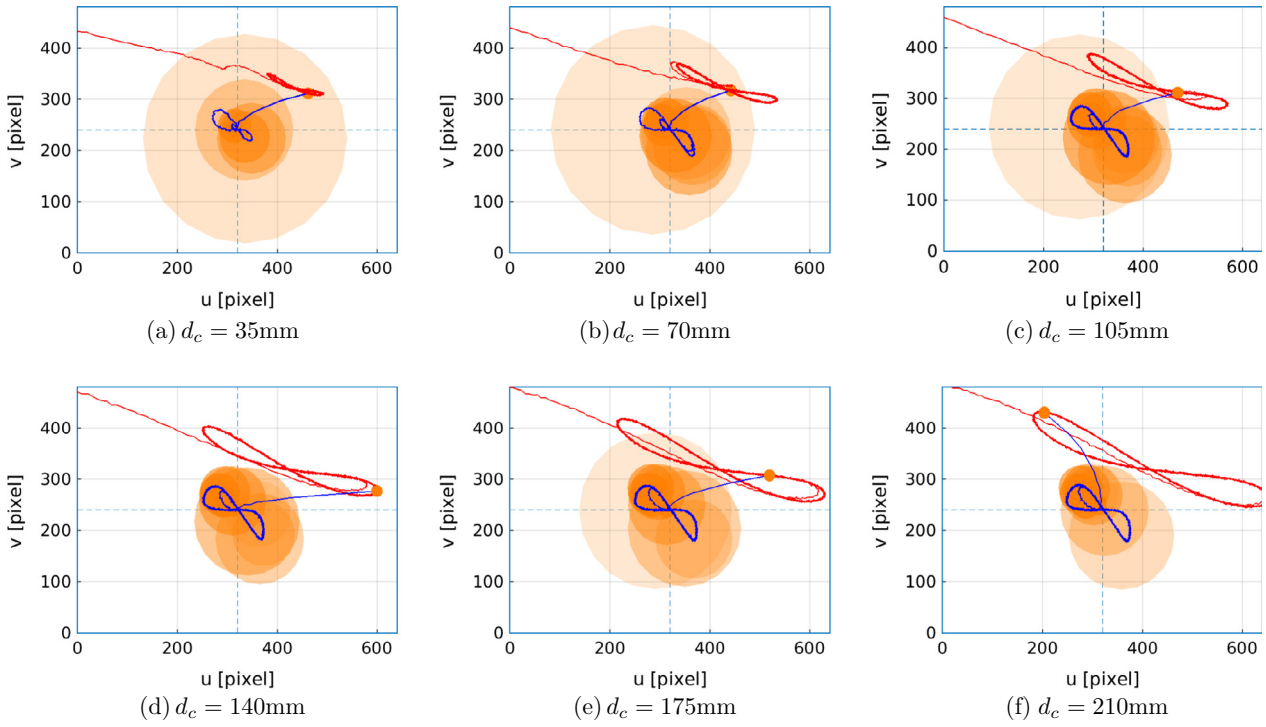

Fig. 4. Non-robust controller: Time-varying fruit position and relative fruit size in the image plane of the camera-in-hand. The trajectories in red and blue refer to the observed fruit position during rotation and translation control, respectively. (For interpretation of the references to color in this figure legend, the reader is referred to the web version of this article.)

Simulation results are shown in Figs. 3–7. Fig. 3 shows the image-space trajectory of the fruit during rotation and translation control using the proposed robust controller. Similarly, Fig. 4 shows the image-space trajectory of the fruit using a non-robust controller (i.e., controller with no robust feedback terms). The relative fruit size in the image plane at different times during translation control is also shown (darker to lighter). The rotation controller brings the fruit in the CIH's FOV (red line). It should be noted that at the end of rotation control the deviation of the fruit from the image center is due to uncertainty in the estimated fruit depth and the fruit motion. Once the fruit is in the FOV, the robust translation controller regulates the fruit close to the image center (blue line) as shown in Fig. 3. Fig. 4 shows undesirable oscillatory behavior using the non-robust controller that exacerbates with increase in fruit motion.

The rotation and translation error plots using the robust and the non-robust controller for $d_c = 140$ mm are shown in Figs. 5 and 6. It can be seen from Figs. 5(a) and 6(a) that the rotation and translation errors are reduced to arbitrarily small value using the robust controller. Also, from Fig. 6(a), it is evident that the robot approaches the fruit only after the image-space error $\|e_{v1}(t)\|$ becomes arbitrarily small. This guarantees that the fruit will remain close to the image center as robot reaches the moving fruit. On the other hand, the non-robust controller shows sustained oscillations in the image-space error $e_{v1}(t)$, and consequently in the depth regulation error $e_{v2}(t)$ (see Fig. 6(b)). The sustained oscillations may result in lower harvesting efficiency due to unsuccessful harvest attempts.

The time-varying trajectory of the end-effector along with the time-varying fruit position using the proposed robust controller is shown in Fig. 7. It can be observed that during rotation control the optical axis of the CIH (green arrow) is aligned to point in the direction of the target fruit. The translation controller subsequently servos the end-effector to the target fruit in the presence of unknown fruit motion (blue line).

8. Experimental validation

8.1. Testbed

The performance of the developed robust visual servo controller was validated in an indoor experiment using a Robotics Research K-1607 manipulator shown in Fig. 8(a). The K-1607 is a 7-axis, kinematically-redundant, electric-drive articulated robotic arm. The arm is fitted with a three finger servo-actuated gripper that also accommodates the CIH (KT&C, KPCS20-CP1) and an IR proximity sensor as shown in Fig. 8(b). The function of the IR sensor is to activate the gripper mechanism when the robot is sufficiently close to the target fruit. A Sony FCB-EX780S "block" camera mounted in the robot's workspace served as a fixed camera. Both the cameras were calibrated using Caltech Camera Calibration Toolbox and the calibration matrices were obtained as

$$A = \begin{bmatrix} 382.23 & 0 & 162.11 \\ 0 & 383.80 & 114.83 \\ 0 & 0 & 1 \end{bmatrix}, \quad A_f = \begin{bmatrix} 436.06 & 0 & 155.85 \\ 0 & 437.19 & 119.57 \\ 0 & 0 & 1 \end{bmatrix}. \tag{58}$$

Images captured by the cameras were digitized using USB frame grabbers. The image processing workstation (IPW) identified fruits from the captured images using image thresholding, and the Euclidean position of the identified fruits was estimated with respect to $\mathcal{F}_f$ using (5). Based on the obtained fruit position, the rotation control input in (12) and, subsequently, the translation control input in (20) and (23) was obtained to regulate the end-effector to the fruit position. The robot control workstation (RCW) generated the lower level joint torque commands based on the desired control velocity input from the IPW. Also, the RCW broadcasted the joint position feedback along with the end-effector position and orientation to the IPW through a real-time communication network.

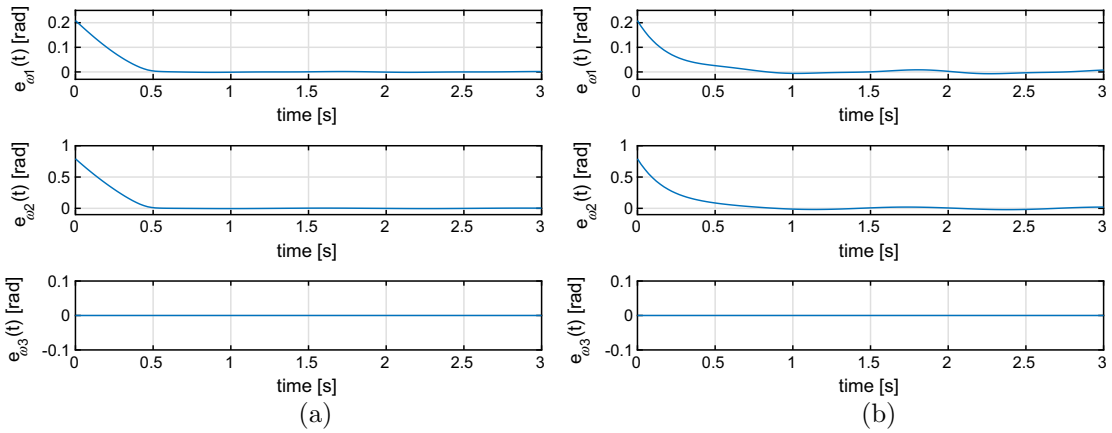

Fig. 5. Rotation error $e_\omega(t) = [e_{\omega 1}(t)\ e_{\omega 2}(t)\ e_{\omega 3}(t)]^T$ for $d_c = 140$ mm using (a) the proposed robust controller and (b) without robust feedback terms.

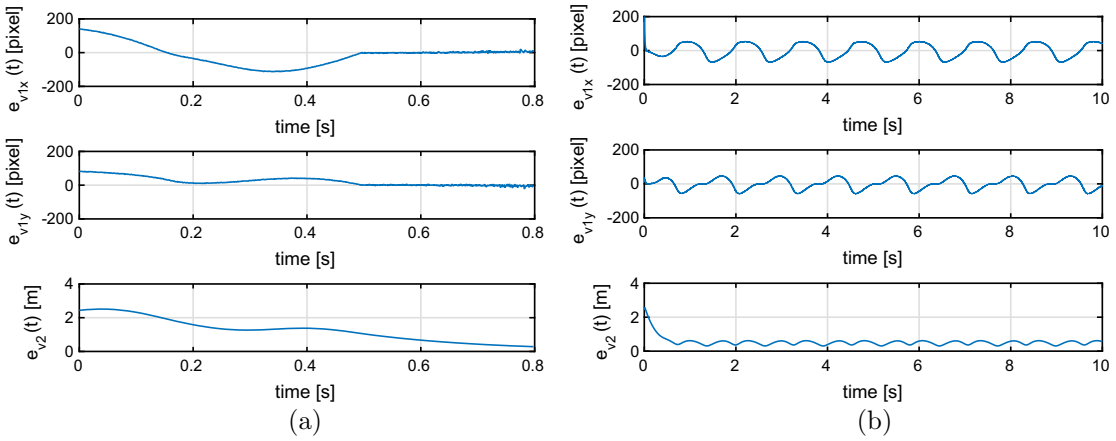

Fig. 6. Translation error $e_v(t) = [e_{v1}^T(t)\ e_{v2}(t)]^T$ for $d_c = 140$ mm, where $e_{v1}(t) = [e_{v1x}(t)\ e_{v1y}(t)]^T$ using (a) the proposed robust controller and (b) without robust feedback terms.

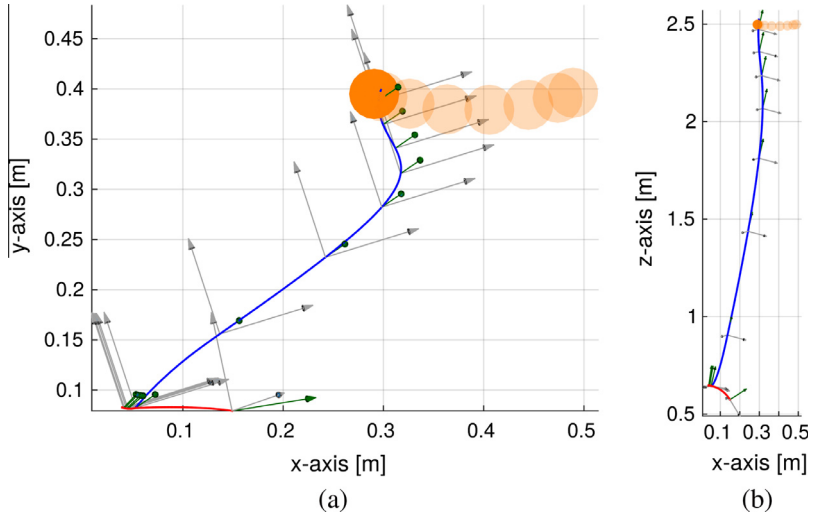

Fig. 7. Euclidean plot showing the motion of the target fruit and the end-effector trajectory in *xy* and *xz*-planes. The trajectories in red and blue show the position of the end-effector during rotation control and translation control, respectively. The green arrow represents the direction of the optical axis of the camera. (For interpretation of the references to color in this figure legend, the reader is referred to the web version of this article.)

We used an artificial citrus fruit suspended in the air using a string to imitate a fruit attached to a stem. The fruit was manually perturbed in the experiment and the performance of the controller with and without robust feedback elements was recorded. The displacement of the fruit centroid was ≈ 120 mm. The constants in (12), (20), and (23) were selected as

Fig. 8. (a) Robotic Research K-1607 manipulator and (b) three finger gripper with the CIH located inside the end-effector.

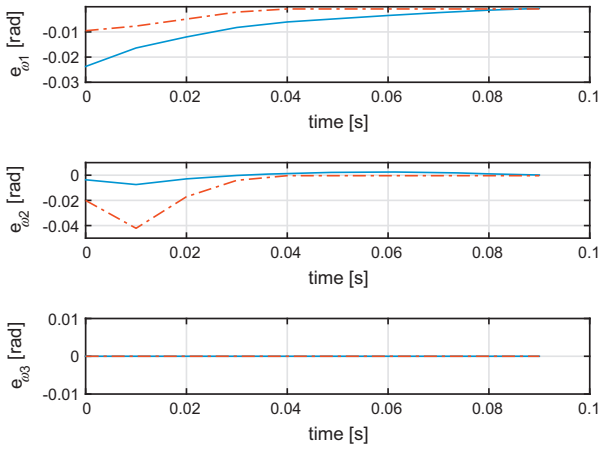

Fig. 9. Rotation error $e_\omega(t) = [e_{\omega 1}(t)\ e_{\omega 2}(t)\ e_{\omega 3}(t)]^T$ using the proposed robust controller (blue line) and without robust feedback terms (red dash-dot line). (For interpretation of the references to color in this figure legend, the reader is referred to the web version of this article.)

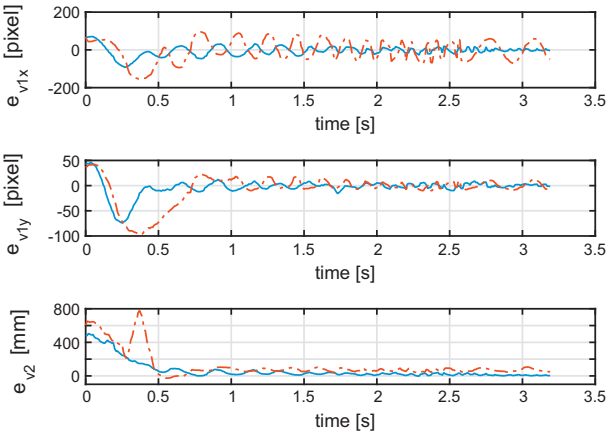

Fig. 10. Translation error $e_v(t) = [e_{v1}^T(t)\ e_{v2}(t)]^T$, where $e_{v1}(t) = [e_{v1x}(t)\ e_{v1y}(t)]^T$ using the proposed robust controller (blue line) and without robust feedback terms (red dash-dot line). (For interpretation of the references to color in this figure legend, the reader is referred to the web version of this article.)

$$k_\omega = 4, \quad \gamma_\omega = 2, \quad \epsilon_\omega = 0.1, \tag{59}$$

$$k_p = 2, \quad k_z = 3, \quad \epsilon_p = 5, \quad \epsilon_z = 10, \tag{60}$$

$$\gamma_p = 50, \quad \gamma_d = 10, \quad \alpha = 1, \quad w = 0.5. \tag{61}$$

8.2. Results

The rotation and translation error plots are shown in Figs. 9 and 10, respectively. Similar to simulations results in Section 7, the non-robust controller shows sustained oscillations in the image x and y-directions (red dash-dot line). Since (20) includes the excitation term $w\|e_{v1}\|^2$, the end-effector in non-robust control does not regulate to the desired depth as seen in the plot of $e_{v3}(t)$ in Fig. 10. It can be seen from Figs. 9 and 10 that the robust controller (blue solid line) offers excellent disturbance rejection and the errors approach arbitrarily close to the equilibrium point. In addition, the robust controller does not show strong oscillatory behavior which is seen in the non-robust controller. The reduced position error would translate into less unsuccessful pick cycles or improved picking efficiency. Thereby, reinforcing the benefit of active disturbance rejection. The position of the fruit in the image plane of the CIH during translation control is shown in Fig. 11. The fruit is regulated close to the center of the image while the end-effector is driven to the desired depth. Fig. 12 shows the relative position of the target fruit expressed in the CIH coordinate frame. From Figs. 11 and 12, it can be seen that even in the presence of unknown fruit motion the fruit is regulated along the optical axis of the CIH at the desired depth for harvesting.

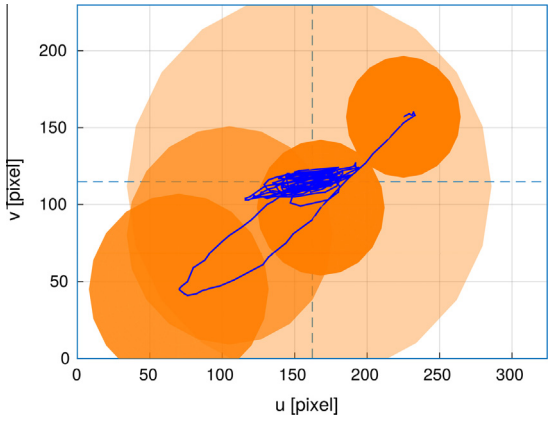

Fig. 11. Time-varying fruit position in the image plane of the camera-in-hand. The trajectories in red and blue refer to the observed fruit position during rotation and translation control, respectively. The relative size of the fruit in the image plane at different time instances during translation control is also shown. (For interpretation of the references to color in this figure legend, the reader is referred to the web version of this article.)

9. Conclusion

Arising from the practical challenge to compensate unknown fruit motion due to wind gust, canopy unloading, and particularly, fruit detachment forces, a nonlinear robust visual servo controller is developed. The unknown fruit motion is included in the system dynamics as a nonlinear non-vanishing disturbance to actively compensate for the motion. In-depth control formulation and

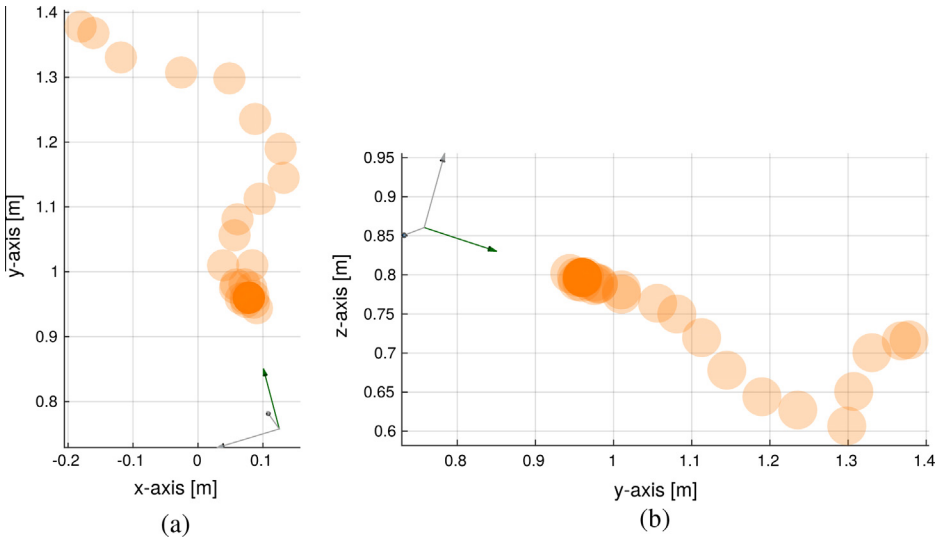

Fig. 12. Euclidean plot showing the relative position of the target fruit observed in the CIH coordinate frame. The green arrow represents the direction of the optical axis of the camera. (For interpretation of the references to color in this figure legend, the reader is referred to the web version of this article.)

rigorous stability analysis guarantee uniformly ultimately bounded regulation of the end-effector to the desired position. Finite time convergence analysis is presented to obtain maximum pick cycle time. Moreover, a desired pick cycle time or fruit removal rate can be obtained by "tuning" the control gains following the guidelines presented in the paper. Extensive simulation with varying fruit motions and a proof-of-concept experiment demonstrate stable closed-loop operation of the system and indicate satisfactory performance of the proposed robust controller in disturbance rejection.

Appendix A. Nomenclature

$\mathcal{F}$	camera-in-hand coordinate frame
$\mathcal{F}_f$	fixed camera coordinate frame
$\mathcal{F}_b$	stationary robot base frame
$\bar{m}(t) = [x(t)\ y(t)\ z(t)]^T$	fruit coordinates in $\mathcal{F}$
$\bar{m}_f(t) = [x_f(t)\ y_f(t)\ z_f(t)]^T$	fruit coordinates in $\mathcal{F}_f$
$\hat{\bar{m}}(t) = [\hat{x}(t)\ \hat{y}(t)\ \hat{z}(t)]^T$	estimated fruit coordinates in $\mathcal{F}$
$\hat{\bar{m}}_f(t) = [\hat{x}_f(t)\ \hat{y}_f(t)\ \hat{z}_f(t)]^T$	estimated fruit coordinates in $\mathcal{F}_f$
$\hat{\bar{m}}'(t)$	estimated fruit coordinates $\hat{\bar{m}}_f(t)$ expressed in $\mathcal{F}$
$p(t) = [u(t)\ v(t)]^T$	fruit image coordinates in $\mathcal{F}$
$p_f(t) = [u_f(t)\ v_f(t)]^T$	fruit image coordinates in $\mathcal{F}_f$
A	camera-in-hand calibration matrix
A_f	fixed camera calibration matrix
$p_d = [u_0\ v_0]^T$	coordinates of the principal point
z_d	desired fruit depth expressed in $\mathcal{F}$
$v_c(t) = \left[v_c'(t)^T\ v_{cz}(t)\right]^T$	linear velocity of the camera-in-hand
$\omega_c(t)$	angular velocity of the camera-in-hand
$v_r(t)$	linear velocity of the end-effector
$\omega_r(t)$	angular velocity of the end-effector
$e_\omega(t)$	rotation error
$u(t), \theta(t)$	angle–axis representation of $e_\omega(t)$
$e_{v1}(t)$	translation error (image dynamics)
$e_{v2}(t)$	translation error (depth dynamics)
$d_\omega(t)$	component of fruit motion affecting rotation dynamics
$d_p(t)$	component of fruit motion affecting image dynamics
$d_z(t)$	component of fruit motion acting along the optical axis
$\gamma_\omega \geqslant \|d_\omega(t)\|$	upper bound on $d_\omega(t)$
$\gamma_p \geqslant \|d_p(t)\|$	upper bound on $d_p(t)$
$\gamma_d \geqslant \|d_z(t)\|$	upper bound on $d_z(t)$
k_ω	rotation controller gain
k_p	translation controller gain (image dynamics)
k_z	translation controller gain (depth dynamics)
$\epsilon_\omega, \epsilon_p, \epsilon_z$	arbitrarily small positive constants
α	positive constant such that $\alpha\hat{z} \geqslant z$
ξ	constant ratio $\hat{z}/z$
w	positive weight on the term $\|e_{v1}(t)\|^2$
$e_{\omega\infty}, e_{v1\infty}, e_{v2\infty}$	error ball corresponding to $e_\omega(t), e_{v1}(t), e_{v2}(t)$, respectively.

Appendix B. Practical challenges

In this section, some of the practical challenges pertaining to vision-based robotic harvesting systems are discussed, and the corresponding merits and demerits of the developed controller are identified.

B.1. Illumination, shadows, partial occlusion

Environmental factors such as uneven illumination, shadows cast by branches and leaves, and partial fruit occlusion may lead to partial fruit detection, where only a part of the fruit is identified. In Mehta and Burks (2014b), we presented an analysis to characterize robustness of the controller to partial fruit detection in the absence of fruit motion. An extension of these results is presented to analyze the effect of partial fruit detection on the performance of the developed robust controller.

The estimated fruit position $\hat{\bar{m}}'(t)$ in the CIH coordinate frame $\mathcal{F}$ can be related to the true fruit position $\bar{m}_{f_{\text{true}}}(t)$ expressed in $\mathcal{F}_f$ by Mehta and Burks (2014b)

$$\hat{\bar{m}}'(t) = R_r^{-1}\left(R_{ef}A_f^{-1}\chi_u A_f \bar{m}_{f_{\text{true}}} + t_{ef} - t_r\right) \tag{B.1}$$

where $R_{ef} \in \mathbb{R}^{3\times3}$ and $t_{ef} \in \mathbb{R}^3$ denote the known constant rotation and translation of frame $\mathcal{F}_f$ with respect to $\mathcal{F}_b$, $R_r(t) \in \mathbb{R}^{3\times3}$ and $t_r(t) \in \mathbb{R}^3$ denote the known time-varying rotation and translation of $\mathcal{F}$ with respect to $\mathcal{F}_b$, and $\chi_u \in \mathbb{R}^{3\times3}$ is given by

$$\chi_u = \begin{bmatrix} \gamma_x\gamma_z & 0 & 0 \\ 0 & \gamma_y\gamma_z & 0 \\ 0 & 0 & \gamma_z \end{bmatrix} \tag{B.2}$$

where $\gamma_x, \gamma_y \in \mathbb{R}_{>0}$ is the uncertainty in the measured fruit centroid in the image plane such that

$$\begin{bmatrix} p_f^T & 1 \end{bmatrix}^T = \frac{\chi_u}{\gamma_z}\begin{bmatrix} p_{f_{\text{true}}}^T & 1 \end{bmatrix}^T \tag{B.3}$$

and $\gamma_z \geqslant 1$ is the uncertainty in fruit depth estimation due to partial fruit detection such that $\hat{z}_f = \gamma_z z_{f\text{true}}$.

B.1.1. Rotation controller

The performance of the rotation controller in the presence of uncertainty χ_u due to partial fruit detection needs to be analyzed. At large, the aim is to find under which conditions the target fruit will be visible to the CIH at the end of rotation control.

From (33), and using the absolute homogeneity of the norm function,

$$\lim_{t\to\infty} \|e_\omega\| = \lim_{t\to\infty} \theta(t) \leqslant e_{\omega\infty} \tag{B.4}$$

where $\|u(t)\| = 1$ and $0 \leqslant \theta \leqslant \pi$ are used. Therefore, at the end of rotation control, the target fruit coordinates can be guaranteed to be in the following compact set:

$$B_{\hat{\bar{m}}'} = \left\{\hat{x}'^2 + \hat{y}'^2 \leqslant \hat{r}'^2\sin^2(e_{\omega\infty}), \hat{r}'\cos(e_{\omega\infty}) \leqslant \hat{r}'\right\}. \tag{B.5}$$

In (B.5), $\hat{r}'(t) = \|\hat{\bar{m}}'(t)\|$. Consider the worst-case scenario when the target fruit coordinates at the end of rotation control, denoted by $\hat{\bar{m}}'_\infty \in \mathbb{R}^3$, are given by

$$\lim_{t\to\infty} \hat{\bar{m}}' = \hat{\bar{m}}'_\infty = \begin{bmatrix} \frac{\hat{r}'\sin(e_{\omega\infty})}{\sqrt{2}} & \frac{\hat{r}'\sin(e_{\omega\infty})}{\sqrt{2}} & \hat{r}'\cos(e_{\omega\infty}) \end{bmatrix}^T. \tag{B.6}$$

The compact set B_1 containing the image coordinates $\hat{p}'_\infty \in \mathbb{R}^2$ corresponding to $\hat{\bar{m}}'_\infty$ can be obtained using (B.5) and (B.6) as

$$B_1 = \left\{\hat{u}'^2_\infty + \hat{v}'^2_\infty \leqslant f^2\tan^2(e_{\omega\infty})\right\} \tag{B.7}$$

where $\hat{u}'_\infty, \hat{v}'_\infty \in \mathbb{R}$ are the image x and y-coordinates of $\hat{p}'_\infty$, and $f \in \mathbb{R}$ is the constant known focal length of the CIH.

Using (B.1) and (B.6), the true position, $\bar{m}_{\text{true}}(t)$, of the fruit in the CIH coordinate frame at the end of rotation control can be obtained as

$$\lim_{t\to\infty} \bar{m}_{\text{true}}(t) = R_r^{-1}\left(R_{ef}A_f^{-1}\chi_u^{-1}A_f R_{ef}^{-1}\left(R_r\hat{\bar{m}}'_\infty - t_{ef} + t_r\right) + t_{ef} - t_r\right). \tag{B.8}$$

It can be verified from (B.8) that in the absence of uncertainty, i.e., $\chi_u = I_3$, the true and the estimated fruit positions coincide, i.e., $\bar{m}_{\text{true}} = \hat{\bar{m}}'_\infty$. The virtual image coordinates $p_{\text{true}}(t)$ corresponding to $\bar{m}_{\text{true}}$ can be obtained as

$$p_{\text{true}} = \frac{1}{z_{\text{true}}}A\bar{m}_{\text{true}}. \tag{B.9}$$

where $z_{\text{true}} \in \mathbb{R}$ is the true depth of the target fruit from the CIH. It can be seen from (B.9) that, as $t \to \infty$, any deviation in $\bar{m}_{\text{true}}$ from $\hat{\bar{m}}'_\infty$ due to uncertainties χ_u will result in deviation of p_{true} from set B_1.

To view the fruit, the image coordinates p_{true} are only required to lie in the FOV of the CIH. Therefore, the rotation controller is inherently tolerant to uncertainties due to partial fruit detection. Further, from (B.9), the robustness to position uncertainty depends on the camera calibration parameters of the CIH, such that the robustness to partial fruit detection can be improved by selecting a camera with short focal length (i.e., wide FOV).

The robustness of the developed rotation controller is demonstrated using an example where the depth uncertainty γ_z due to partial fruit detection is varied between 1.0 and 1.3, i.e., up to about 40% of the fruit may not detected. Since in (B.9) the image coordinates p_{true} are functions of the fruit depth, z_{true} is varied from 500 to 2000 mm. The results are shown in Fig. B.13; Fig. B.13a shows the true image position p_{true} of the fruit as a function of γ_z for various fruit depths z_{true}; Fig. B.13b shows the deviation of p_{true} from the image center, where the error $e(t)$ is defined as $e \triangleq p_d - p_{\text{true}}$.

In the second example, the depth uncertainty is kept constant at $\gamma_z = 1.2$, and the uncertainty in the of fruit centroid, γ_x and γ_y, is varied between 0.8 and 1.2. The results are shown in Fig. B.14; Fig. B.14a shows the image position p_{true} of the fruit as a function of γ_x and γ_y for various depths z_{true}; Fig. B.14b shows the deviation of p_{true} from the image center.

It can be seen from Fig. B.14a that the fruit remains in the camera FOV for most γ_x, γ_y, and z_{true}. From Figs. B.13a and B.14a, the

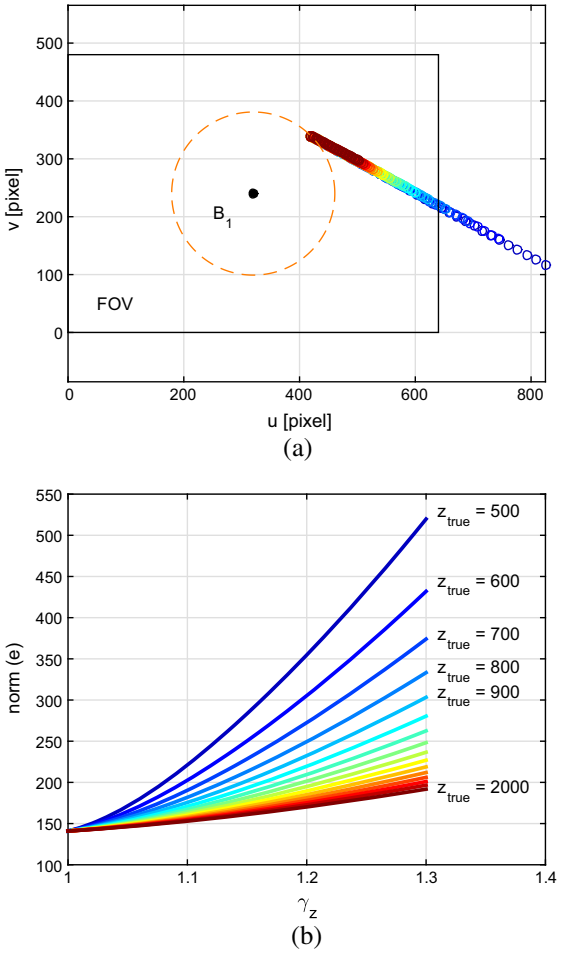

Fig. B.13. (a) The true image coordinates p_{true} of a fruit as a function of depth uncertainty γ_z for various fruit depths. (b) Deviation in the true image coordinates, p_{true}, from the image center.

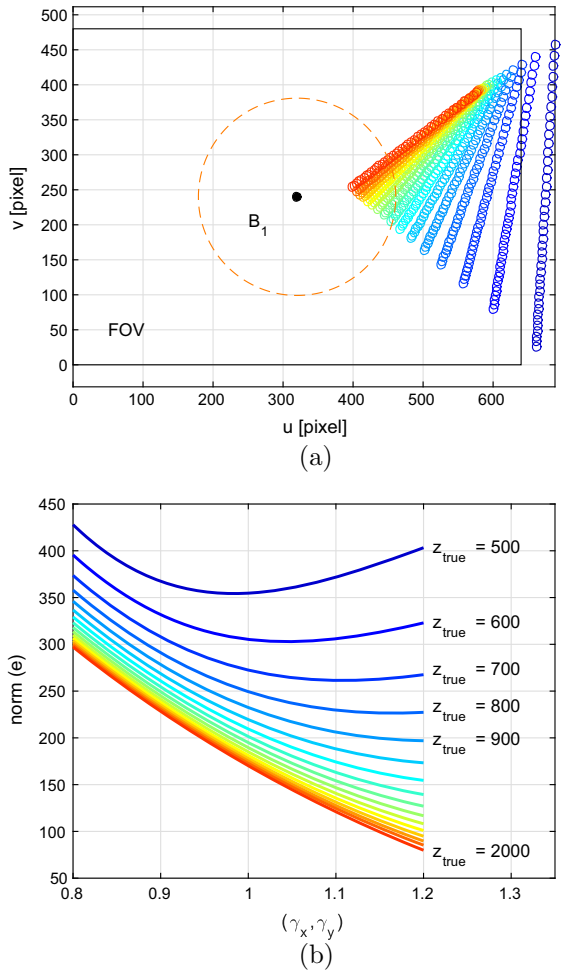

Fig. B.14. (a) The true image coordinates p_{true} of a fruit as a function of γ_x and γ_y for various fruit depths. (b) Deviation in the true image coordinates, p_{true}, from the image center.

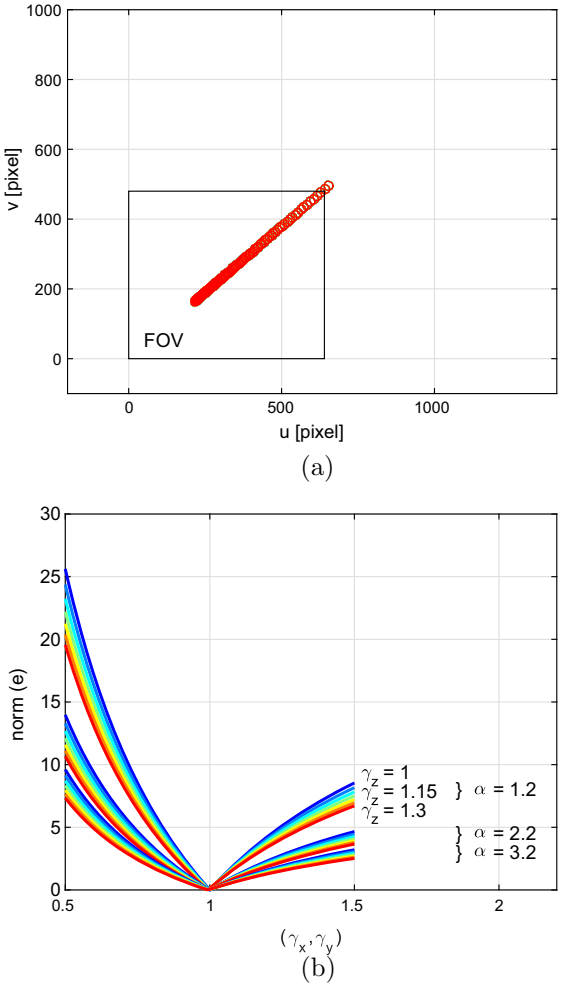

Fig. B.15. (a) The true image coordinates p_{true} of a fruit as a function of γ_x and γ_y for various fruit depths. (b) Deviation in the true image coordinates, p_{true}, from the image center.

robustness of the rotation controller is observed to degrade with decrease in the initial fruit depth z_{true} of the CIH, which is evident from (B.9).

B.1.2. Translation controller

Robustness of translation controller to partial fruit detection can be analyzed with respect to the developed controllers in (20) and (23). In (20), the linear velocity $v_{cz}(t)$ along the optical axis guarantees the end-effector is regulated such that the estimated fruit depth $\alpha\hat{z}$ approaches the constant desired depth z_d. From the fact that $\hat{z}(t) = \gamma_z z_{\text{true}}(t)$ for $\gamma_z \geqslant 1$ and $\alpha\hat{z}(t) \geqslant z_{\text{true}}(t)$, the controller (20) is robust to depth estimation errors from partial fruit detection. Moreover, robustness can be improved by selecting α arbitrarily large such that the end-effector is guaranteed to reach the actual fruit depth.

The controller in (23) uses only the image measurements to regulate the fruit image coordinates to the image center. Therefore, (23) is robust to depth estimation error γ_z. Let us analyze the effect of uncertainties γ_x and γ_y on the performance of the controller in (23). Using (B.9) and based on uncertainty formulation in (B.3), the true Euclidean position of the target fruit in the CIH coordinate frame can be related to observed image coordinates as

$$\bar{m}_{\text{true}} = z_{\text{true}} A^{-1} \begin{bmatrix} \gamma_x & 0 & 0 \\ 0 & \gamma_y & 0 \\ 0 & 0 & 1 \end{bmatrix}^{-1} \begin{bmatrix} p^T & 1 \end{bmatrix}^T. \tag{B.10}$$

From (41) and (47), the translation controller in (20) and (23) regulates the end-effector with respect to the target fruit to a compact set given below

$$B_{p,\hat{z}} = \left\{ (u_\infty - u_0)^2 + (v_\infty - v_0)^2 \leqslant e_{v1\infty}^2, \quad |\alpha\hat{z} - z_d| \leqslant e_{v2\infty} \right\} \tag{B.11}$$

where $u_\infty, v_\infty \in \mathbb{R}$ denote the x and y components of $p(t)$ as $t \to \infty$.

Assuming the error $e_{v1\infty}$ to be equally distributed in the image x and y directions and considering the worst case scenario when the target fruit lies on the boundary of the compact set in (B.11), the true position of the fruit in (B.10) as $t \to \infty$ can be written as

$$\lim_{t\to\infty} \bar{m}_{\text{true}} = \frac{z_d + e_{v2\infty}}{\alpha\gamma_z} A^{-1} \begin{bmatrix} \gamma_x & 0 & 0 \\ 0 & \gamma_y & 0 \\ 0 & 0 & 1 \end{bmatrix}^{-1} \begin{bmatrix} p_d^T + \begin{bmatrix} \frac{e_{v1\infty}}{\sqrt{2}} & \frac{e_{v1\infty}}{\sqrt{2}} \end{bmatrix} & 1 \end{bmatrix}^T. \tag{B.12}$$

In the absence of uncertainties and exogenous disturbances, the true position of the target fruit should be along the optical axis of the camera. Therefore, it can be seen from (B.12) that the robustness to uncertainties γ_x and γ_y can be improved by selecting α arbitrarily high. This can also be verified from the expression in (46), where the rate of convergence of $\alpha\hat{z}$ to z_d (i.e., the rate of decay of $e_{v2}(t)$) can be improved by increasing α.

Consider an example where γ_x and γ_y are varied from 0.5 to 1.5 while γ_z goes from 1 to 1.3. The results are shown in Fig. B.15; Fig. B.15(a) shows the image position of the fruit as a function of γ_x and γ_y for various γ_z. It can be seen from Fig. B.15(a) that the change in the fruit position in the CIH FOV is independent of the change in γ_z, i.e., the fruit position in the image plane is robust to depth estimation uncertainty. Fig. B.15(b) shows the deviation $e(t)$ of $\bar{m}_{\text{true}}$ from the servoed position given in (B.11). From Fig. B.15(b), it is clear that increasing the constant α can lead to improved robustness to uncertainties.

B.2. Overlapping and clustered fruit

The overlapping and clustered fruit pose an image processing challenge to detect individual fruits from the cluster. Advanced image processing including perimeter detection and shape analysis techniques (Hannan et al., 2009) can be used to identify partially occluded or clustered (i.e., overlapping) fruit. In the presence of overlapping fruit, the depth estimator uses the major and minor axis of the fruit, d_{ix}, d_{iy}, obtained from shape analysis techniques to estimate the fruit depth as listed in Footnote 1. It is to be noted that the controller design remains unchanged in the presence of overlapping fruit.

B.3. Obstacles in the environment

Branches can affect operation of the robotic harvesting system in two ways. The presence of branches may result in partial or complete fruit occlusion. As shown in Appendix B.1, the developed visual servo controller is tolerant to partial fruit detection from partial occlusion. However, branches along the robot trajectory acting as obstacles may affect the performance of the visual servo controller and even damage the end-effector. In an effort to improve dexterity, we are investigating hybrid manipulators with continuum joint end-effectors as well as advanced path planning methods for obstacle avoidance (Mehta and Burks, 2014a).

References

Allen, P.K., Timcenko, A., Yoshimi, B., Michelman, P., 1993. Automated tracking and grasping of a moving object with a robotic hand-eye system. IEEE Trans. Robot. Automat. 9, 152–165.

Bac, C.W., Henten, E.J., Hemming, J., Edan, Y., 2014. Harvesting robots for high-value crops: state-of-the-art review and challenges ahead. J. Field Robot. 31, 888–911.

Baeten, J., Donné, K., Boedrij, S., Beckers, W., Claesen, E., 2008. Autonomous fruit picking machine: a robotic apple harvester. In: Field and Service Robotics. Springer, pp. 531–539.

Buemi, F., Massa, M., Sandini, G., Costi, G., 1996. The agrobot project. Adv. Space Res. 18, 185–189.

Ceres, R., Pons, F.L., Jimenez, A.R., Martin, F.M., Calderon, L., 1998. Design and implementation of an aided fruit-harvesting robot (Agribot). Ind. Robot 25, 337–346.

De-An, Z., Jidong, L., Wei, J., Ying, Z., Yu, C., 2011. Design and control of an apple harvesting robot. Biosyst. Eng. 110, 112–122.

d'Esnon, A.G., 1985. Robotic harvesting of apples. In: Agri-Mation 1. ASAE, Chicago, IL, pp. 210–214.

Edan, Y., Flash, T., Peiper, U., Shmulevich, I., Sarig, Y., 1991. Near-minimum-time task planning for fruit-picking robots. IEEE Trans. Robot. Automat. 7, 48–56.

Fagerer, C., Dickmanns, D., Dickmanns, E.D., 1994. Visual grasping with long delay time of a free floating object in orbit. Auton. Robots 1, 53–68.

Fortuna, L., Muscato, G., Nunnari, G., Pandolfo, A., Plebe, A., 1996. Application of neural control in agriculture: an orange picking robot. Acta Hortic., 441–450

Hannan, M.W., Burks, T.F., 2004. Current developments in automated citrus harvesting, in: ASABE Annual International Meeting, p. ASAE Paper. No. 043087.

Hannan, M.W., Burks, T.F., Bulanon, D.M., 2009. A machine vision algorithm combining adaptive segmentation and shape analysis for orange fruit detection. Agric. Eng. Int.: CIGR EJ. XI, 1–17.

Harrell, R.C., Adsit, P.D., Munilla, R.D., Slaughter, D.C., 1990a. Robotic picking of citrus. Robotica 8, 269–278.

Harrell, R.C., Adsit, P.D., Pool, T.A., Hoffman, R., et al., 1990b. The Florida robotic grove-lab. Trans. ASAE 33, 391–399.

Harrell, R.C., Slaughter, D.C., Adsit, P.D., 1989. A fruit-tracking system for robotic harvesting. Mach. Vis. Appl. 2, 69–80.

Hayashi, S., Ganno, K., Ishii, Y., Tanaka, I., 2002. Robotic harvesting system for eggplants. Jpn. Agric. Res. Quart. 36, 163–168.

Herisse, B., Hamel, T., Mahony, R., Russotto, F.X., 2010. The landing problem of a vtol unmanned aerial vehicle on a moving platform using optical flow. In: 2010 IEEE/RSJ International Conference on Intelligent Robots and Systems (IROS). IEEE, pp. 1600–1605.

Horaud, R., Dornaika, F., Espiau, B., 1998. Visually guided object grasping. IEEE Trans. Robot. Automat. 14, 525–532.

Janabi-Sharifi, F., Wilson, W.J., 1998. Automatic grasp planning for visual-servo controlled robotic manipulators. IEEE Trans. Syst. Man Cybernet. Part B: Cybernet. 28, 693–711.

Jimenez, A., Ceres, R., Pons, J., et al., 2000. A survey of computer vision methods for locating fruit on trees. Trans. ASAE – Am. Soc. Agric. Eng. 43, 1911–1920.

Juste, F., Sevila, F., 1991. Citrus: an European project to study the robotic harvesting of oranges, in: 2nd Workshop on Robotics in Agriculture and Food in Industry, pp. 187–196.

Kondo, N., Nishitsuji, Y., Ling, P., Ting, K., 1996. Visual feedback guided robotic cherry tomato harvesting. Trans. ASAE 39, 2331–2338.

Kragić, D., Miller, A.T., Allen, P.K., 2001. Real-time tracking meets online grasp planning. In: IEEE International Conference on Robotics and Automation, 2001, Proceedings 2001 ICRA. IEEE, pp. 2460–2465.

Levi, P., Falla, A., Pappalardo, R., 1988. Image controlled robotics applied to citrus fruit harvesting. In: 7th International Conference on Robot Vision and Sensory Controls. IFS Publications, Zurich, Switzerland.

Li, P., Lee, S., Hsu, H., 2011. Review on fruit harvesting method for potential use of automatic fruit harvesting systems. Proc. Eng. 23, 351–366.

Malis, E., Chaumette, F., 2002. Theoretical improvements in the stability analysis of a new class of model-free visual servoing methods. IEEE Trans. Robot. Automat. 18, 176–186.

Mehta, S., Ton, C., Kan, Z., Curtis, J., 2015. Vision-based navigation and guidance of a sensorless missile. J. Franklin Inst. 352, 5569–5598.

Mehta, S.S., Burks, T.F., 2014a. Path planning and robust control for robotic citrus harvesting, in: Proc. of the Robotics and associated High-technologies and Equipment for Agriculture and forestry (RHEA), Madrid, Spain, pp. 467–476.

Mehta, S.S., Burks, T.F., 2014b. Vision-based control of robotic manipulator for citrus harvesting. Comput. Electron. Agric. 102, 146–158.

Mehta, S.S., MacKunis, W., Burks, T.F., 2014. Nonlinear robust visual servo control for robotic citrus harvesting, in: IFAC World Congress, pp. 8110–8115.

Mehta, S.S., MacKunis, W., Curtis, J.W., 2011. Adaptive vision-based missile guidance in the presence of evasive target maneuvers, in: 18th IFAC World Congress, pp. 5471–5476.

Muscato, G., Prestifilippo, M., Abbate, N., Rizzuto, I., 2005. A prototype of an orange picking robot: past history, the new robot and experimental results. Ind. Robot: Int. J. 32, 128–138.

Nomura, H., Naito, T., 2000. Integrated visual servoing system to grasp industrial parts moving on conveyer by controlling 6DOF arm. In: 2000 IEEE International Conference on Systems, Man, and Cybernetics. IEEE, pp. 1768–1775.

Plebe, A., Grasso, G., 2001. Localization of spherical fruits for robotic harvesting. Mach. Vis. Appl. 13, 70–79.

Rabatel, G., Bourely, A., Sevila, F., Juste, F., 1995. Robotic harvesting of citrus: state-of-art and development of the French Spanish EUREKA project, in: Proceedings of International conference on Harvest and Post harvest Technologies for Fresh Fruits and Vegetables, pp. 232–239.

Sarig, Y., 1993. Robotics of fruit harvesting: a state-of-the-art review. J. Agric. Eng. 54, 265–280.

Serra, P., Cunha, R., Hamel, T., Cabecinhas, D., Silvestre, C., 2014. Landing on a moving target using image-based visual servo control. In: 2014 IEEE 53rd Annual Conference on Decision and Control (CDC). IEEE, pp. 2179–2184.

Smith, C.E., Papanikolopoulos, N.P., 1997. Grasping of static and moving objects using a vision-based control approach. J. Intell. Robot. Syst. 19, 237–270.

Tillett, N.D., 1993. Robotic manipulators in horticulture: a review. J. Agric. Eng. Res. 55, 89–105.

Van Henten, E.J., Hemming, J., Van Tuijl, B.A.J., Kornet, J.G., Bontsema, J., 2003. Collision-free motion planning for a cucumber picking robot. Biosyst. Eng. 86, 135–144.

Van Henten, E.J., Hemming, J., Van Tuijl, B.A.J., Kornet, J.G., Meuleman, J., Bontsema, J., Van Os, E.A., 2002. An autonomous robot for harvesting cucumbers in greenhouses. Auton. Robots 13, 241–258.

Wang, Y., Zhang, G.l., Lang, H., Zuo, B., De Silva, C.W., 2014. A modified image-based visual servo controller with hybrid camera configuration for robust robotic grasping. Robot. Auton. Syst. 62, 1398–1407.